bioRxiv preprint doi: https://doi.org/10.1101/2020.06.23.162727; this version posted June 23, 2020. The copyright holder for this preprint (which was not certified by peer review) is the author/funder, who has granted bioRxiv a license to display the preprint in perpetuity. It is made available under aCC-BY-NC 4.0 International license.

# Automatic Generation of Personalised Models of the Lower Limb from Three-Dimensional Bone Geometries: A Validation Study

Luca Modenese[1] and Jean-Baptiste Renault[2]

[1] Department of Civil and Environmental Engineering, Imperial College London, UK

[2] Aix-Marseille University, CNRS, ISM UMR 7287, 13009 Marseille, France

CORRESPONDING AUTHOR:

Luca Modenese
Dept of Civil and Environmental Engineering
Room 228B, Skempton Building
Imperial College London
e-mail: l.modenese@imperial.ac.uk

bioRxiv preprint doi: https://doi.org/10.1101/2020.06.23.162727; this version posted June 23, 2020. The copyright holder for this preprint (which was not certified by peer review) is the author/funder, who has granted bioRxiv a license to display the preprint in perpetuity. It is made available under aCC-BY-NC 4.0 International license.


# Abstract

The generation of personalised and patient-specific musculoskeletal models is currently a cumbersome and time-consuming task that normally requires several processing hours and trained operators. We believe that this aspect discourages the use of computational models even when appropriate data are available and personalised biomechanical analysis would be beneficial. In this paper we present a computational tool that enables the fully automatic generation of skeletal models of the lower limb from three-dimensional bone geometries, normally obtained by segmentation of medical images. This tool was validated against four manually created lower limb models finding remarkable agreement in the computed joint parameters, well within human operator repeatability, with the only exception being the subtalar joint axis estimation, which was sensitive to the bone segmentation quality. To prove the robustness of the methodology, the models were built from datasets including both genders, anatomies ranging from juvenile to elderly and bone geometries reconstructed from high-quality computed tomography as well as lower-quality magnetic resonance imaging scans. The entire workflow, implemented in MATLAB scripting language, executed in seconds and required no operator intervention, creating lower extremity models ready to use for kinematic and kinetic analysis or as baselines for more advanced musculoskeletal modelling approaches, of which we provide some practical examples. We auspicate that this technical advancement will promote the use of personalised models in larger-scale studies than those hitherto undertaken.


**Keywords:** Anatomical Coordinate System, Lower Limb, Skeletal Model, Musculoskeletal Model, Kinematics, Three-dimensional bone model, Surface Fitting, 3D Imaging

bioRxiv preprint doi: https://doi.org/10.1101/2020.06.23.162727; this version posted June 23, 2020. The copyright holder for this preprint (which was not certified by peer review) is the author/funder, who has granted bioRxiv a license to display the preprint in perpetuity. It is made available under aCC-BY-NC 4.0 International license.

# 1 Introduction

Musculoskeletal models have proven to be powerful computational tools to study muscle function and internal forces in healthy (Hamner et al., 2010; Saxby et al., 2016) and clinical populations (Barber et al., 2017; Fox et al., 2018; Montefiori et al., 2019b). Recent technical progress in predictive simulation approaches (Dembia et al., 2019; Falisse et al., 2019) has enabled the investigation of if-then scenarios that could support planning and execution of physical interventions. However, applications of personalised medicine often require highly accurate representations of the anatomy of the musculoskeletal system based on medical images such as magnetic resonance imaging (MRI) or computed tomography (CT) scans. For example, accurate models of bone geometries are essential in orthopaedics for planning surgeries and designing personalised surgical equipment (Barrett et al., 2006; Clarke et al., 2018; Jones et al., 2018; Victor and Premanathan, 2013). Personalised (or subject-specific) anatomical models are also of paramount importance in investigations of human motion to ensure accurate estimations of joint kinematics and kinetics (Kainz et al., 2017; Stagni et al., 2000), muscle moment arms (Scheys et al., 2008) and internal forces (Gerus et al., 2013; Lenaerts et al., 2008; Marra et al., 2015).

Previous studies presented methods to generate subject-specific models of the entire lower limb (Marra et al., 2015; Modenese et al., 2018) or individual joints (Barzan et al., 2019; Brito da Luz et al., 2017; Montefiori et al., 2019a; Nardini et al., 2020) and dedicated modelling tools like NMSBuilder (Valente et al., 2017a) or specialized features in the AnyBody software (Damsgaard et al., 2006) are available to implement those workflows. Nevertheless, patient-specific musculoskeletal models are currently employed in small-sized clinical applications (Falisse et al., 2020; Montefiori et al., 2019b; Pitto et al., 2019; Taddei et al., 2012; Valente et al., 2017b), mostly because the generation of each model is a time-demanding operation requiring manual intervention by specialized operators. For example, a codified approach proposed in Modenese et al. (2018) reported around 10 hours to build a complete bilateral musculoskeletal model of the lower limbs from segmented bone geometries, while Scheys et al. (2006) reported on average 65 minutes to define the lower limb musculature using an atlas-based semi-automated approach. We believe that validated and fully automatic workflows are of paramount importance to enable large-scale use of these computational models.

Multiple studies with orthopaedic focus have explored the possibility of defining anatomical coordinate systems (ACSs) in the lower extremity bones based on key geometrical features. Miranda et al. (2010) and Rainbow et al. (2013) proposed fully automatic methods for defining ACSs for the distal femur, proximal tibia and patella, that showed minimum variability with the bone morphology. Kai et al. (2014) developed an automatic approach to identify the reference systems of the pelvis, femur and tibia based on principal axes of inertia, principal component analysis and longitudinal

bioRxiv preprint doi: https://doi.org/10.1101/2020.06.23.162727; this version posted June 23, 2020. The copyright holder for this preprint (which was not certified by peer review) is the author/funder, who has granted bioRxiv a license to display the preprint in perpetuity. It is made available under aCC-BY-NC 4.0 International license.

slicing, obtaining ACSs compatible with those created by human operators, except for the pelvis where anterior tilt was up to 18.8° higher. More recently, Renault et al. (2018) proposed multiple algorithms based on the automatic identification of the articular surfaces at the hip and knee joints, showing high repeatability of these methods when applied on 24 CT scans by three operators. However, in these previous works the ACSs were not defined consistently across publications and none of these methods has been employed for creating articulated skeletal models yet.

Statistical shape modelling workflows have recently demonstrated high potential for reconstructing bone geometries from sparse anatomical datasets (Davico et al., 2019; Nolte et al., 2016; Suwarganda et al., 2019) and landmarks digitized in the gait lab (Nolte et al., 2020; Zhang et al., 2016), but to the best of the authors' knowledge they do not yet offer methods to generate articulated skeletal models of the complete lower limb. The bone reconstructions are limited to the long bones (Nolte et al., 2020; Nolte et al., 2016) or omit the talus and foot bones (Davico et al., 2019; Suwarganda et al., 2019; Zhang et al., 2016), and in musculoskeletal modelling contexts they have been employed to perform non-linear scaling of pre-existing muscle attachments (Nolte et al., 2016) with scarce focus towards joint modelling. Hence, a comprehensive approach to generate entire lower limb models from personalised bone geometries is still missing.

The aim of this paper is to present a tool to create complete models of the complete lower limb from three-dimensional bone geometries in a completely automatic way. The tool implements a workflow that executes in negligible computational time and generates models usable immediately in kinematic and kinetic analyses or employable as baselines for fully featured musculoskeletal models. The models produced by this tool are validated against manually created models that were employed in previous research and the joint parameters computed by competing algorithms are compared to assess their interchangeability. Examples of further technical developments, such as joint articular mechanics and integration with anatomical models of musculature, are finally provided to demonstrate the tool's potential for enabling large-scale studies and broader musculoskeletal research.

# 2 Materials and methods

## 2.1 Workflow to generate automatic skeletal models

A set of computational methods proposed in previous literature to define ACSs automatically (Kai et al., 2014; Miranda et al., 2010; Renault et al., 2018) were acquired and included in a more extensive modelling workflow. The geometrical methods from Renault et al. (2018), available in the public "GIBOC-KNEE" MATLAB toolbox, were forked directly from the GitHub repository (https://github.com/renaultJB/GIBOC-Knee-Coordinate-System) and extensively modified and expanded, while the methods described by Kai et al. (2014) were independently reimplemented and

bioRxiv preprint doi: https://doi.org/10.1101/2020.06.23.162727; this version posted June 23, 2020. The copyright holder for this preprint (which was not certified by peer review) is the author/funder, who has granted bioRxiv a license to display the preprint in perpetuity. It is made available under aCC-BY-NC 4.0 International license.

those of Miranda et al. (2010) were obtained through contacting the authors of the publication. Additional algorithms were developed *ad hoc* for the purposes of this investigation (Table 1).

The implemented workflow (Figure 1) consisted of the following steps: a) obtaining segmented three-dimensional bone geometries of the pelvis, femur, patella, tibia, fibula, talus, calcaneus and the other foot bones from medical images; b) automatically processing these bone models to extract the geometrical parameters required to define ACSs and appropriate joint coordinate systems (JCSs) for the parent and child bodies of each joint of the lower limb; c) creating an articulated skeletal model of the lower limb in OpenSim format (Delp et al., 2007) using the identified JCSs and ACSs.

In step b), bone geometries were analysed starting with a transformation to the ACSs defined by their principal axes of inertia (Gonzalez-Ochoa et al., 1998; Mirtich, 1996), followed by bone-specific features extraction. The complete list of algorithms available to define each JCS is reported in Table 1 and the details of the methodologies are described in their reference publications, and for the newly developed algorithms for the pelvis, talus and foot, in the supplementary materials. The articulated skeletal models were generated leveraging the MATLAB (The MathWorks, Natick, MA, USA) application programming interface (API) of OpenSim 4.1 (Seth et al., 2018): a rigid body with appropriate inertial properties (Winter, 2009) was created for each leg segment and a *SpatialTransform* for each joint based on the JCSs identified at step c). The individual JCSs, consistent with Modenese et al. (2018), are described in Table 1. For convenience in the validation step, all rigid bodies shared a local coordinate system that was coincident with that of the medical images, as they would have in a model generated using NMSBuilder. The lower limb models included five bodies: pelvis, femur, tibia (including fibula and a rigidly attached patella), talus and foot (including calcaneus and foot bones), and five joints: a free joint between pelvis and ground, a ball and socket joint for the hip joint and hinge joints for the tibiofemoral, talocrural and subtalar joints. The models also included fourteen landmarks (Table 2) automatically identified on the bone surfaces and intended for registration with the skin markers used in standard gait analysis.

The entire set of scripts implementing this workflow was organized in a MATLAB toolbox named STAPLE (S*hared* T*ools for* A*utomatic* P*ersonalised* L*ower* E*xtremity modelling*).

## 2.2 Validation of automatic models

The models produced by the automatic tool were validated against musculoskeletal models of the lower limb generated for other purposes using NMSBuilder (*manual models)* and previously employed in published research (Montefiori et al., 2019b) or contributions at international conferences (Modenese et al., 2020; Modenese et al., 2019). These subject-specific models were built following the codified approach of Modenese et al. (2018) and using bone geometries available in public datasets plus an *in vivo* MRI dataset collected with the approval of the Imperial College Research

bioRxiv preprint doi: https://doi.org/10.1101/2020.06.23.162727; this version posted June 23, 2020. The copyright holder for this preprint (which was not certified by peer review) is the author/funder, who has granted bioRxiv a license to display the preprint in perpetuity. It is made available under aCC-BY-NC 4.0 International license.

Ethics Committee. A complete description of the datasets, characterized by quality of the bone geometry meshes ranging from very good (LHDL-CT) to low (JIA-MRI), is provided in Table 3 and Figure 2.

Articulated skeletal models for all datasets were generated using the STAPLE toolbox (*automatic models*) and their JCSs compared against those of the manual models, reporting differences in their origin location and axes orientation. These quantities were evaluated in the common global coordinate system of the medical images. The automatic models were created using algorithms that resembled the manual approach (pelvis: STAPLE-pelvis, femur: GIBOC-Cylinder, tibia: Kai-Tibia, talus: STAPLE-Talus and foot: STAPLE-Foot). It is worth noting that not all JCSs in the model were independent, as detailed in their description (Table 1).

### 2.3 Comparison of joint parameters estimated by different algorithms

The JCSs of those joints for which more than one algorithm was available (ground-pelvis and knee joint) were then calculated using all the available options and the resulting JCSs compared to those employed in the validation part of the study, used as reference. Linear distances between origins and angular differences between axes were quantified and expressed in the JCS of the reference algorithm.

## 3 Results

All the automatic models employed in the study were successfully generated in less than 30s each using a standard Z640 Dell Workstation (RAM: 64 GB, CPU: 2 Intel Xeon E5-2630 2.40 GHz).

The comparison of automatic and manual models (Table 4) resulted in an overall strong similarity of the joint parameters across all considered datasets. The hip and talocrural joint centres were in excellent agreement with the manual estimations (maximum errors hip: 0.5 mm, talocrural: 1.2mm), whereas the maximum error was 2.5 mm at the knee joint and 5.9 mm at the subtalar joint in the JIA-MRI model due to the low quality of bone reconstruction (error range in the other datasets: 0.4-3.2 mm). The cranial-caudal position of the pelvis-ground joint origin differed by up to 4.9 mm (range: 0.8-4.9 mm) causing minor differences in pelvic tilt (range: 1.8°-3.6°, see Figure 3-A) that propagated to the hip-parent JCS. The axes of the knee and talocrural hinge joints (medio-lateral Z axes) were estimated with maximum differences from manual models of 1.0° degree, while the subtalar joint axes presented maximum differences up to 2.9° in the datasets with good quality bone geometries but reached 11.3° in the JIA-MRI model (Figure 3-B).

When comparing competing algorithms for the same joints, we observed that differences among their JCSs were not always negligible (Table 5). The Kai-Pelvis algorithm presented larger pelvic tilt offsets than STAPLE-Pelvis, due to different identification of the anterior superior iliac spines, while the posterior landmarks were coincident. The Miranda-Femur algorithm failed twice but also provided

bioRxiv preprint doi: https://doi.org/10.1101/2020.06.23.162727; this version posted June 23, 2020. The copyright holder for this preprint (which was not certified by peer review) is the author/funder, who has granted bioRxiv a license to display the preprint in perpetuity. It is made available under aCC-BY-NC 4.0 International license.

the knee-parent JCSs closest to the reference algorithm together with GIBOC-Spheres, for which differences were smaller than 1° for all cases except JIA-MRI. Kai-Femur and GIBOC-Ellipsoid resulted in more posteriorly and anteriorly located JCSs respectively, with maximum angular differences for the knee joint axis up to 4.7° (LHDL-CT) for the former and 5.2° (TLEM2-CT) for the latter.

At the proximal tibia, all GIBOC algorithms computed more proximal origins than Kai-Tibia's (range: 5.8-12.5 mm), with angular differences in the range 0.5°-11.5° for the medio-lateral axis but smaller for the proximal-distal axis (range: 0.9°-2.9°). Overall, GIBOC-Plateau and Miranda-Tibia, which failed processing TLEM2-CT, identified similar JCSs, as expected by their very similar algorithms. The JCSs from GIBOC-Ellipse and GIBOC-Centroids were also found more similar to each other than to the Kai-Tibia reference.

# 4 Discussion

The aim of this paper was to present a tool to automatically create personalised models of the lower limb from three-dimensional bone geometries segmented in medical images. To validate the proposed methodology, we generated four automatic models and compared them against models manually created from the same data in other research projects. We employed anatomical datasets representative of both genders and a wide range of ages that included bone geometries of various quality derived from both CT and MRI scans (Table 3). We found that the automatic and manual models were remarkably similar (Table 4), with largest differences observed for the pelvis-ground and subtalar joints. In the pelvis, the JCS origin was misplaced by up to 4.9 mm cranially due to the identified bony landmarks (Figure 3-A). This error causes a systematic anterior tilt offset in the range 1.8°-3.6° that would propagate to the hip joint flexion-extension angle in kinematic analysis (see an example in supplementary materials). Although not negligible, this offset represents a substantial improvement (almost 15°) compared to the results reported by Kai et al. (2014). Since our implementation of Kai-Pelvis also yielded smaller pelvic tilt than the original publication, it is likely that their results were affected by considering the sacrum bone in the analysis and using the pubic symphysis to define the JCS. More recent algorithms, e.g. Fischer et al. (2019), could be considered for future additional comparisons. The automatic subtalar joint axis was the other joint parameter for which we observed, although only in the JIA-MRI dataset, a noticeable difference from the equivalent manual model (11.3°, Figure 3-B). This discrepancy appeared to be caused by the low-quality of the talus bone reconstruction since in all the other models the same axis was estimated within 2.9°.

It is worth noting that the differences between JCSs of automatic and manual models were compatible with the human inter-operator variability reported as standard deviations in previous literature. The ranges of origin displacements and joint axes angular differences observed at the hip, knee and

bioRxiv preprint doi: https://doi.org/10.1101/2020.06.23.162727; this version posted June 23, 2020. The copyright holder for this preprint (which was not certified by peer review) is the author/funder, who has granted bioRxiv a license to display the preprint in perpetuity. It is made available under aCC-BY-NC 4.0 International license.

talocrural joint (referred to as "ankle joint" in some publications) were well within the ranges of inter-operator repeatability reported by previous investigations (Hannah et al., 2017; Martelli et al., 2014; Montefiori et al., 2019b) and even the largest difference observed at the subtalar axis was close to the maximum inter-operator variability (9.6°) reported by Montefiori et al. (2019a). Although further investigation is needed to confirm this, based on previous studies (Kainz et al., 2016; Martelli et al., 2014; Montefiori et al., 2019a; Valente et al., 2014) it is reasonable to expect minimal differences in joint angles and moments calculated by manual and automatic models presenting such similar JCSs. Indeed, that was the case when simulating the gait data made available by Montefiori et al. (2019a) with the JIA-MRI manual and automatic model (see supplementary materials). Moreover, simulation results obtained using the STAPLE models will have zero inter- and intra- operator variability due to model construction because of the automatic nature of their generation.

In the validation part of the study the JCSs of all models were defined as in Modenese et al. (2018) for consistency, but we considered other algorithms (Table 1) to enable different modelling approaches. At the pelvis, using Kai-Pelvis instead of STAPLE-Pelvis resulted in larger displacements between the automatic and manual JCSs origins and consequently larger pelvis tilt offsets, suggesting that using the pelvis largest convex hull instead of the principal axes of inertia is a better approach to identify its anterior bony landmarks. For the long bones, JCSs estimated by different algorithms exhibited variability comparable with Renault et al. (2018), that was using bone segmentations from CT scans. At the distal femur the differences observed among JCSs were small (<5° in the 93% of estimations) but not negligible, therefore the choice of the algorithm, e.g. fitting ellipsoids (Sholukha et al., 2011) or spheres (Yin et al., 2015) to the femoral condyles articular surface, must be justified with careful functional anatomy considerations relevant to the research question. At the proximal tibia, the mechanical axis (Y axis) was similar between Kai-Tibia and GIBOC algorithms (range: 0.9°-2.9°) but less for Miranda-Tibia (up to 7°). Larger differences among algorithms were observed in the medio-lateral axis (range: 0.5°-11.5°) and anterior-posterior axis (range: 1.9°-11.7°). Despite this variability, it is interesting to note that the tibiofemoral alignment, i.e. the angle between knee-parent and knee-child medio-lateral Z axis, was 5.7°±3.8° external rotation across all algorithms for the *in vivo* MRI datasets, which is compatible, although slightly larger, with the offset in tibiofemoral alignment observed by Hirschmann et al. (2015) comparing upright and supine non-weight-bearing CT scans in 26 patients (2.7°±5.1° and 2.6°±5.6° external rotation, from two readers). This suggests that the automated methods could be used to correct tibial alignment offsets introduced in standard imaging, although further investigations are required to identify the most suited adjustment algorithm. Finally, in this study the algorithms of Miranda et al. (2010) failed to process some of the datasets. However, it must be considered that a) we plug them in our workflow with minimal modifications and b) we used rather different input data than those they were intended to process, i.e. partial bone reconstructions from high resolution CT scans.

bioRxiv preprint doi: https://doi.org/10.1101/2020.06.23.162727; this version posted June 23, 2020. The copyright holder for this preprint (which was not certified by peer review) is the author/funder, who has granted bioRxiv a license to display the preprint in perpetuity. It is made available under aCC-BY-NC 4.0 International license.

A current limitation of the study is that our validation datasets were only four, and despite their heterogeneity, did not include bone geometries presenting abnormalities or deformities that could be encountered clinically. This limitation is partially mitigated by the availability of multiple algorithms usable in place of a failing one, but additional validation is undoubtedly required before creating automatic models from pathological skeletal anatomies. An additional limitation of use could be the availability of partial bone reconstructions, e.g. from CT scans aiming to minimize exposure to ionizing radiations (Henckel et al., 2006) or in amputees' studies. In fact, this is not an issue for the long bones (femur and tibia) because some algorithms were specifically developed for working with incomplete geometries (Miranda et al., 2010; Renault et al., 2018). Incomplete bone models, however, may represent an obstacle to the identification of the muscle attachments when the aim is generating a complete musculoskeletal model. This issue can be solved by combining the STAPLE toolbox with a statistical shape workflow to reconstruct entire bone geometries from sparse datasets (Nolte et al., 2016; Suwarganda et al., 2019). It is worth mentioning that, although statistical shape modelling workflows present the advantage of reconstructing bone geometries from sparse segmentations or even skin landmarks, bone models from medical image segmentation still provide the most accurate estimations of joint parameters; for example, median root-mean-squared errors up to 11.09 mm (Zhang et al., 2016) and larger than 13.8 mm (Nolte et al., 2020) have been reported in the identification of the centre of the femoral head using statistical shape models. Considering that radiological scans are routinely collected to plan musculoskeletal surgical interventions and that the time required to segment bones (Noguchi et al., 2020) has decreased by orders of magnitudes thanks to recent deep learning techniques, the generation of personalised lower limb models in a number of clinical applications appears technically feasible.

The implemented MATLAB tool is intentionally modular and can automate the generation of entire or partial lower limb models; for example it can be easily modified to produce models of the ankle complex similar to Montefiori et al. (2019a), as demonstrated in the supplementary materials. Moreover, the GIBOC and STAPLE algorithms make available a large amount of anatomical information such as articular surfaces (Figure 4-A) and bone profiles that can be used for implementing more advanced joint models than those proposed here, e.g. contact models (Brandon et al., 2017; Conconi et al., 2015; Smith et al., 2018) or parallel mechanisms (Sancisi and Parenti-Castelli, 2011). Current work is focusing on a robust implementation of a personalised patellofemoral joint similar to Barzan et al. (2019).

It is worth noting that extending skeletal models with models of muscle anatomy can also be completely automated (Modenese and Kohout, 2020). In a previous contribution (Modenese et al., 2020) we have used a non-rigid iterative closest point registration (Audenaert et al., 2019) to map the muscle attachment areas from a cadaveric dataset to the ICL-MRI participant's bones, generating highly-discretized, personalised muscle representations from segmented muscle geometries and

bioRxiv preprint doi: https://doi.org/10.1101/2020.06.23.162727; this version posted June 23, 2020. The copyright holder for this preprint (which was not certified by peer review) is the author/funder, who has granted bioRxiv a license to display the preprint in perpetuity. It is made available under aCC-BY-NC 4.0 International license.

simulating their kinematics during gait (Figure 4-B). Future efforts will focus on streamlining these methodologies towards a comprehensive, fully automated, modelling tool for generating subject-specific musculoskeletal models.

In summary, this work presents a computational tool enabling researchers to generate articulated, subject-specific skeletal models of the lower limb in negligible time through a completely automatic workflow that takes three-dimensional bone geometries as inputs. These models can be used immediately for kinematic and kinetic analyses or can serve as extendable baselines for complete musculoskeletal models including musculotendon actuators. This work is framed in a long-term plan aiming to advance the state of the art of anatomical modelling and promote large-scale clinical adoption of personalised computational models of the musculoskeletal system through complete automation of the most challenging modelling tasks.

All the models and scripts used in this investigation will be made available for download at https://simtk.org/projects/auto-sk-models after publication of the manuscript.

## CRediT authorship contribution statement

**Luca Modenese:** Conceptualization, Methodology, Software, Data Curation, Validation, Formal analysis, Writing – original draft, Writing – review and editing.

**Jean-Baptiste Renault:** Investigation, Software, Writing – review and editing.

## Acknowledgements

LM was supported by an Imperial College Research Fellowship granted by Imperial College London. The authors want to thank Dr Michael Rainbow for making available the MATLAB code employed in the Miranda-Femur and Miranda-Tibia algorithms. LM wants to thank Metin Bicer, Arnault Caillet, Bobby Zhang, Clement Favier and Andrew Phillips for the feedback on the manuscript.

## Conflict of interest statement

The authors declare that they do not have any financial or personal relationship with other people or organizations that could have inappropriately influenced this study.

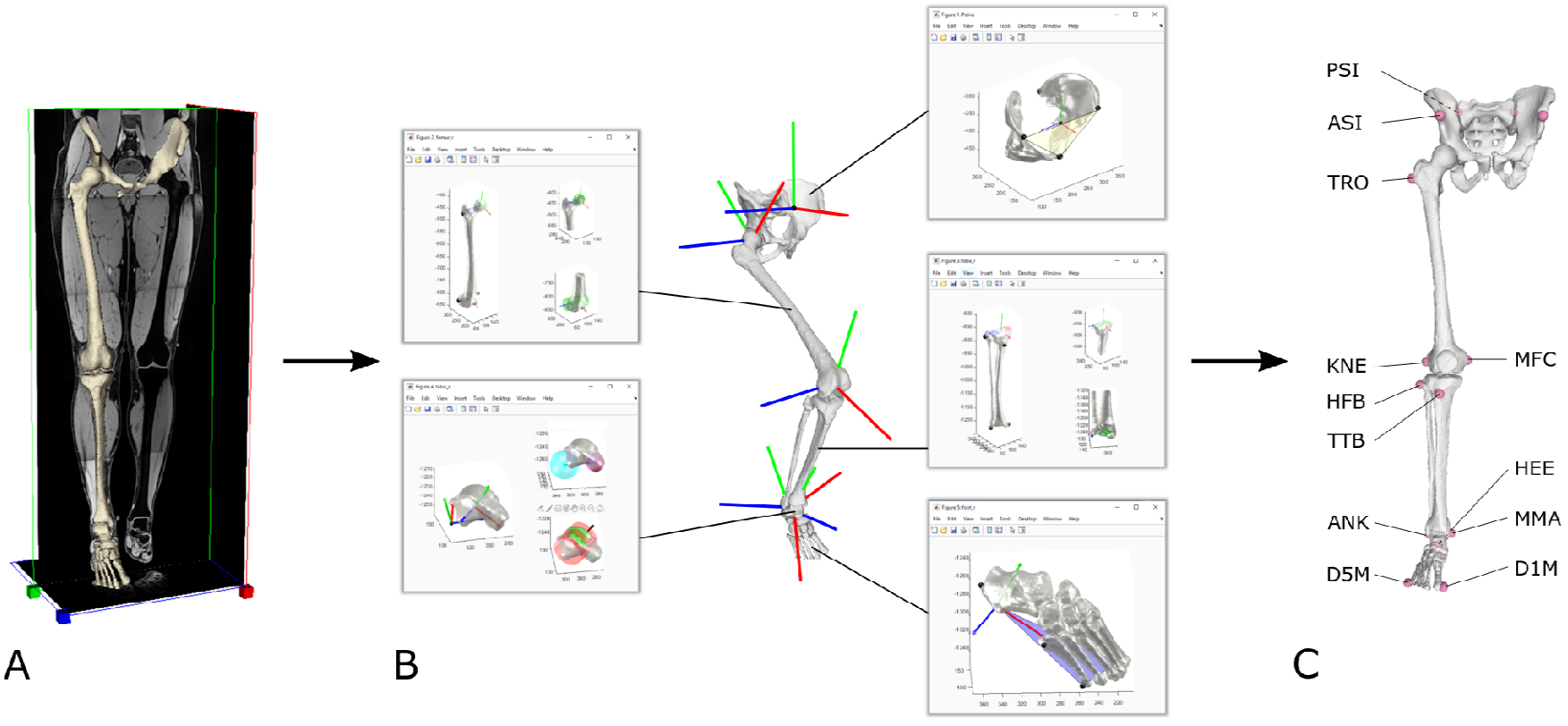


Figure 1 Workflow for automatic generation of articulated skeletal models: the three-dimensional bone geometries segmented from medical images (A) are fed to a MATLAB toolbox that computes the joint coordinate systems (B) used to assemble a fully functional OpenSim model inclusive of the most common bony landmarks used in gait analysis (C). For clarity only the child joint reference systems are shown in (B) for all joints.



bioRxiv preprint doi: https://doi.org/10.1101/2020.06.23.162727; this version posted June 23, 2020. The copyright holder for this preprint (which was not certified by peer review) is the author/funder, who has granted bioRxiv a license to display the preprint in perpetuity. It is made available under aCC-BY-NC 4.0 International license.

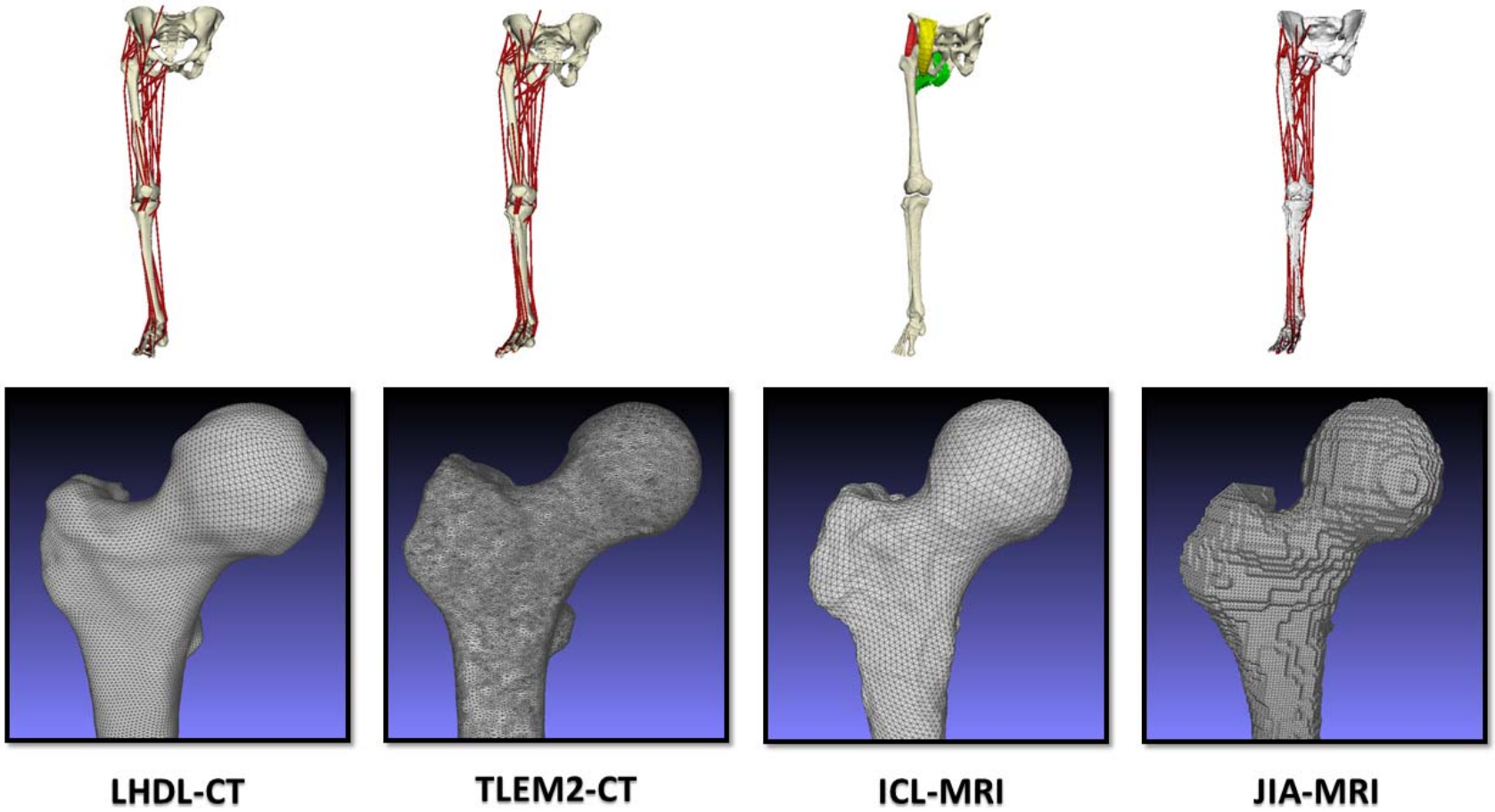


Figure 2 Musculoskeletal models of the lower limb from previous research used for validating the automatically generated skeletal models (first row). The models were built using bone reconstructions of variable quality (second row). Details about these models are available in Table 3.



bioRxiv preprint doi: https://doi.org/10.1101/2020.06.23.162727; this version posted June 23, 2020. The copyright holder for this preprint (which was not certified by peer review) is the author/funder, who has granted bioRxiv a license to display the preprint in perpetuity. It is made available under aCC-BY-NC 4.0 International license.

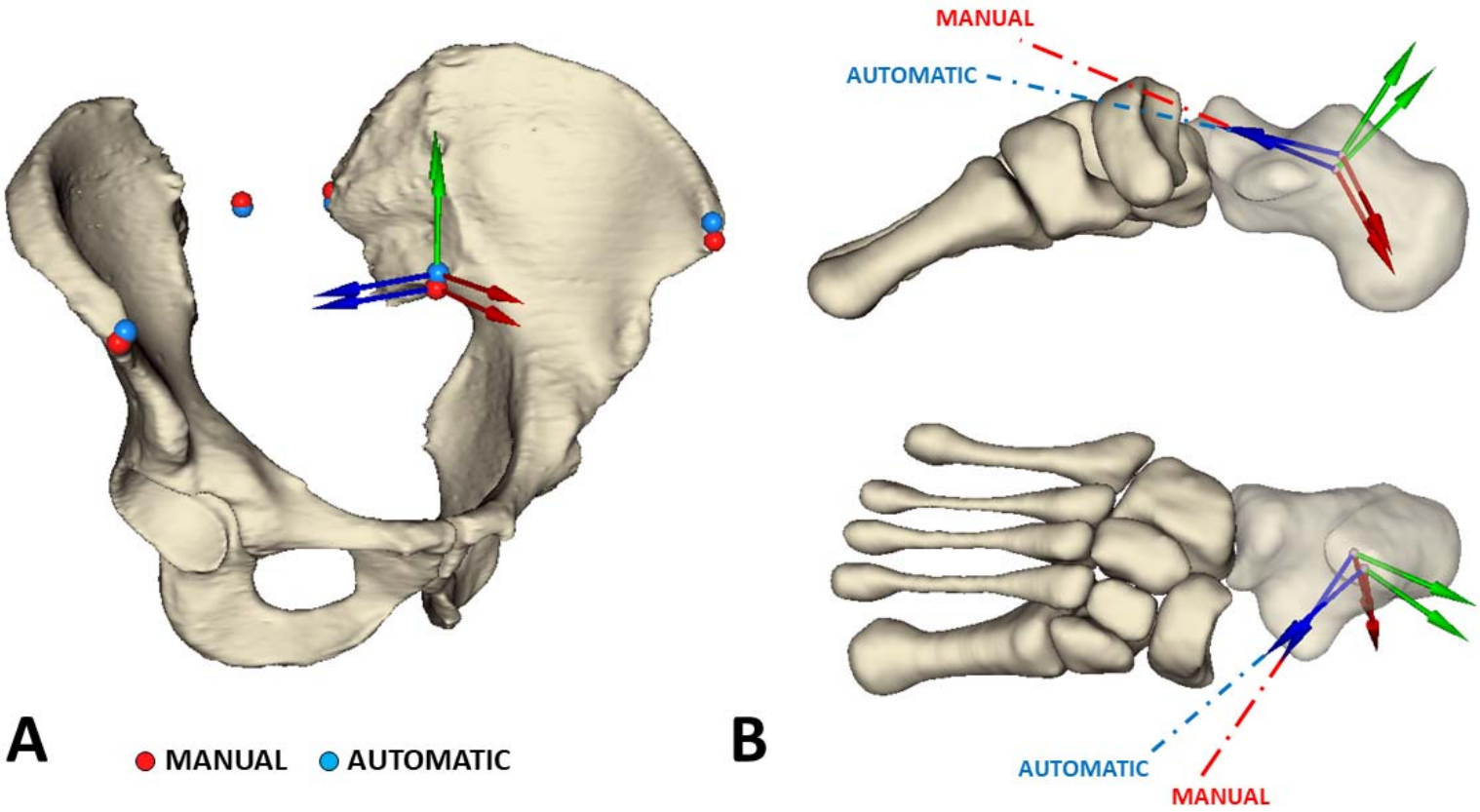


Figure 3 Maximum differences between manual and automatic models found at the pelvis-ground joint of TLEM2-CT using the STAPLE-Pelvis algorithm (A) and at the JIA-MRI subtalar joint using the STAPLE-Talus algorithm(B).



bioRxiv preprint doi: https://doi.org/10.1101/2020.06.23.162727; this version posted June 23, 2020. The copyright holder for this preprint (which was not certified by peer review) is the author/funder, who has granted bioRxiv a license to display the preprint in perpetuity. It is made available under aCC-BY-NC 4.0 International license.

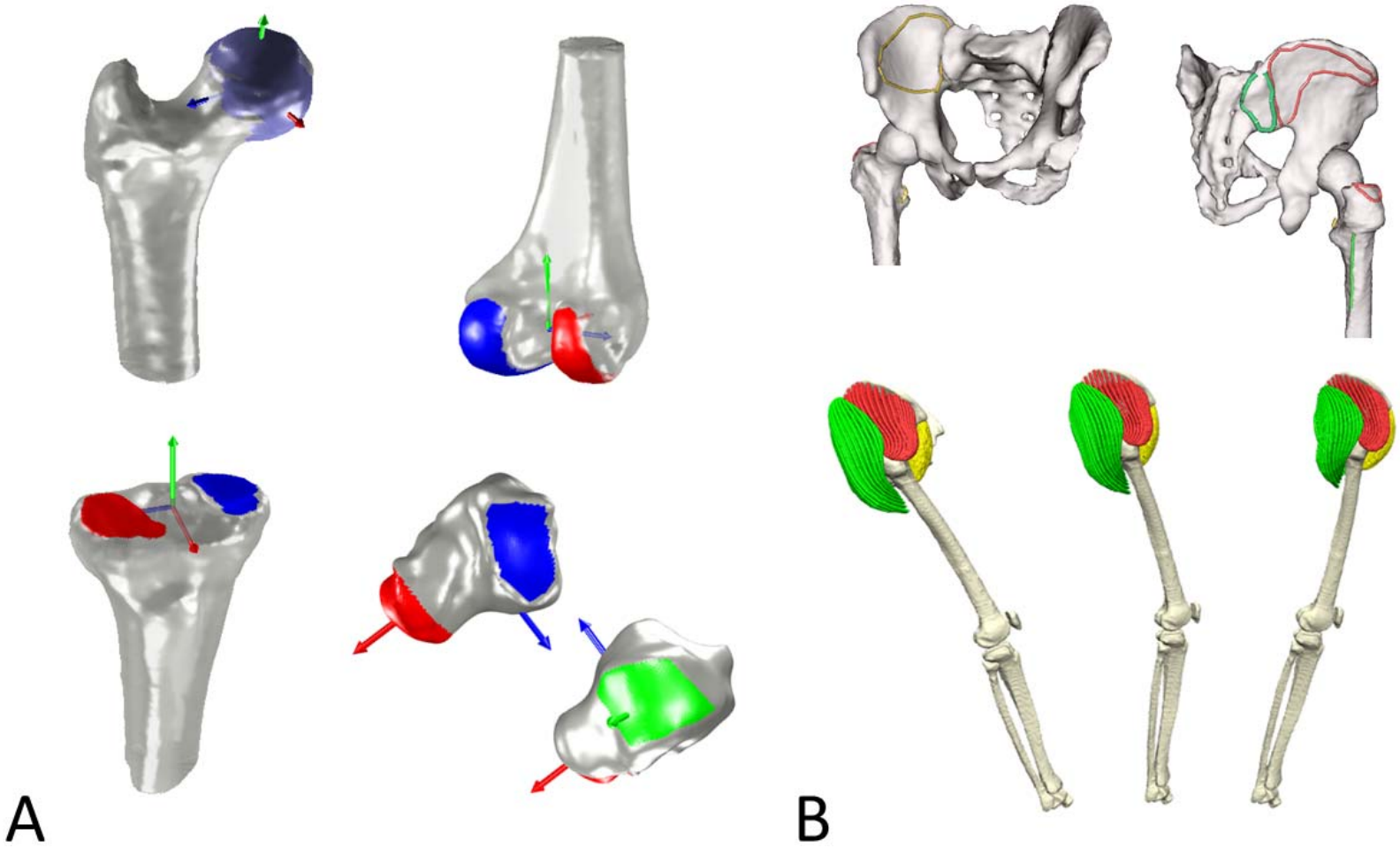


Figure 4 Examples of articular surfaces identified at the femur, tibia and talus by the automatic algorithms (A) and example of augmentation of the ICL-MRI lower extremity model using an automatically generated subject-specific hip musculature including muscle fibres and attachment areas (B).



bioRxiv preprint doi: https://doi.org/10.1101/2020.06.23.162727; this version posted June 23, 2020. The copyright holder for this preprint (which was not certified by peer review) is the author/funder, who has granted bioRxiv a license to display the preprint in perpetuity. It is made available under aCC-BY-NC 4.0 International license.

bioRxiv preprint doi: https://doi.org/10.1101/2020.06.23.162727; this version posted June 23, 2020. The copyright holder for this preprint (which was not certified by peer review) is the author/funder, who has granted bioRxiv a license to display the preprint in perpetuity. It is made available under aCC-BY-NC 4.0 International license.

# References

Audenaert, E.A., Van Houcke, J., Almeida, D.F., Paelinck, L., Peiffer, M., Steenackers, G., Vandermeulen, D., 2019. Cascaded statistical shape model based segmentation of the full lower limb in CT. Computer Methods in Biomechanics and Biomedical Engineering 22, 644-657.

Barber, L., Carty, C., Modenese, L., Walsh, J., Boyd, R., Lichtwark, G., 2017. Medial gastrocnemius and soleus muscle□tendon unit, fascicle, and tendon interaction during walking in children with cerebral palsy. Developmental Medicine & Child Neurology 59, 843-851.

Barrett, A.R.W., Davies, B.L., Gomes, M.P.S.F., Harris, S.J., Henckel, J., Jakopec, M., Rodriguez y Baena, F.M., Cobb, J.P., 2006. Preoperative planning and intraoperative guidance for accurate computer-assisted minimally invasive hip resurfacing surgery. Proceedings of the Institution of Mechanical Engineers, Part H: Journal of Engineering in Medicine 220, 759-773.

Barzan, M., Modenese, L., Carty, C.P., Maine, S., Stockton, C.A., Sancisi, N., Lewis, A., Grant, J., Lloyd, D.G., da Luz, S.B., 2019. Development and validation of subject-specific pediatric multibody knee kinematic models with ligamentous constraints. Journal of biomechanics 93, 194-203.

Brandon, S.C., Smith, C.R., Thelen, D.G., 2017. Simulation of soft tissue loading from observed movement dynamics, Handbook of Human Motion. Springer, pp. 1-34.

Brito da Luz, S., Modenese, L., Sancisi, N., Mills, P.M., Kennedy, B., Beck, B.R., Lloyd, D.G., 2017. Feasibility of using MRIs to create subject-specific parallel-mechanism joint models. Journal of Biomechanics 53, 45-55.

Clarke, S., Cobb, J., Jaere, M., Jones, G., Kley, K., Lobenhoffer, P., McCrum, C., Musahl, V., Takeuchi, R., 2018. Osteotomies: Advanced and Complex Techniques, ESSKA Instructional Course Lecture Book. Springer, pp. 129-151.

Conconi, M., Leardini, A., Parenti-Castelli, V., 2015. Joint kinematics from functional adaptation: A validation on the tibio-talar articulation. Journal of Biomechanics 48, 2960-2967.

Damsgaard, M., Rasmussen, J., Christensen, S.T., Surma, E., de Zee, M., 2006. Analysis of musculoskeletal systems in the AnyBody Modeling System. Simulation Modelling Practice and Theory 14, 1100-1111.

Davico, G., Pizzolato, C., Killen, B.A., Barzan, M., Suwarganda, E.K., Lloyd, D.G., Carty, C.P., 2019. Best methods and data to reconstruct paediatric lower limb bones for musculoskeletal modelling. Biomechanics and Modeling in Mechanobiology.

Delp, S.L., Anderson, F.C., Arnold, A.S., Loan, P., Habib, A., John, C.T., Guendelman, E., Thelen, D.G., 2007. OpenSim: open-source software to create and analyze dynamic simulations of movement. IEEE Transactions on Biomedical Engineering 54, 1940-1950.

Dembia, C.L., Bianco, N.A., Falisse, A., Hicks, J.L., Delp, S.L., 2019. OpenSim Moco: Musculoskeletal optimal control. BioRxiv, 839381.

Falisse, A., Pitto, L., Kainz, H., Hoang, H., Wesseling, M., Van Rossom, S., Papageorgiou, E., Bar-On, L., Hallemans, A., Desloovere, K., Molenaers, G., Van Campenhout, A., De Groote, F., Jonkers, I., 2020. Physics-Based Simulations to Predict the Differential Effects of Motor Control and Musculoskeletal Deficits on Gait Dysfunction in Cerebral Palsy: A Retrospective Case Study. Frontiers in Human Neuroscience 14.

Falisse, A., Serrancolí, G., Dembia, C.L., Gillis, J., Jonkers, I., De Groote, F., 2019. Rapid predictive simulations with complex musculoskeletal models suggest that diverse healthy and pathological human gaits can emerge from similar control strategies. Journal of The Royal Society Interface 16, 20190402.

bioRxiv preprint doi: https://doi.org/10.1101/2020.06.23.162727; this version posted June 23, 2020. The copyright holder for this preprint (which was not certified by peer review) is the author/funder, who has granted bioRxiv a license to display the preprint in perpetuity. It is made available under aCC-BY-NC 4.0 International license.

Fischer, M.C.M., Krooß, F., Habor, J., Radermacher, K., 2019. A robust method for automatic identification of landmarks on surface models of the pelvis. Scientific Reports 9, 13322.

Fox, A.S., Carty, C.P., Modenese, L., Barber, L.A., Lichtwark, G.A., 2018. Simulating the effect of muscle weakness and contracture on neuromuscular control of normal gait in children. Gait & posture 61, 169-175.

Gerus, P., Sartori, M., Besier, T.F., Fregly, B.J., Delp, S.L., Banks, S.A., Pandy, M.G., D'Lima, D.D., Lloyd, D.G., 2013. Subject-specific knee joint geometry improves predictions of medial tibiofemoral contact forces. Journal of Biomechanics 46, 2778-2786.

Gonzalez-Ochoa, C., McCammon, S., Peters, J., 1998. Computing moments of objects enclosed by piecewise polynomial surfaces. ACM Transactions on Graphics 17, 143-157.

Hamner, S.R., Seth, A., Delp, S.L., 2010. Muscle contributions to propulsion and support during running. Journal of Biomechanics 43, 2709-2716.

Hannah, I., Montefiori, E., Modenese, L., Prinold, J., Viceconti, M., Mazzà, C., 2017. Sensitivity of a juvenile subject-specific musculoskeletal model of the ankle joint to the variability of operator-dependent input. Proceedings of the Institution of Mechanical Engineers, Part H: Journal of Engineering in Medicine 231, 415-422.

Henckel, J., Richards, R., Lozhkin, K., Harris, S., Baena, F.R.y., Barrett, A., Cobb, J., 2006. Very low-dose computed tomography for planning and outcome measurement in knee replacement. The Journal of bone and joint surgery. British volume 88, 1513-1518.

Hirschmann, A., Buck, F.M., Fucentese, S.F., Pfirrmann, C.W., 2015. Upright CT of the knee: the effect of weight-bearing on joint alignment. European radiology 25, 3398-3404.

Jones, G.G., Jaere, M., Clarke, S., Cobb, J., 2018. 3D printing and high tibial osteotomy. EFORT Open Reviews 3, 254-259.

Kai, S., Sato, T., Koga, Y., Omori, G., Kobayashi, K., Sakamoto, M., Tanabe, Y., 2014. Automatic construction of an anatomical coordinate system for three-dimensional bone models of the lower extremities – Pelvis, femur, and tibia. Journal of Biomechanics 47, 1229-1233.

Kainz, H., Carty, C.P., Maine, S., Walsh, H.P., Lloyd, D.G., Modenese, L., 2017. Effects of hip joint centre mislocation on gait kinematics of children with cerebral palsy calculated using patient-specific direct and inverse kinematic models. Gait & posture 57, 154-160.

Kainz, H., Modenese, L., Lloyd, D.G., Maine, S., Walsh, H.P.J., Carty, C.P., 2016. Joint kinematic calculation based on clinical direct kinematic versus inverse kinematic gait models. Journal of Biomechanics 49, 1658-1669.

Lenaerts, G., De Groote, F., Demeulenaere, B., Mulier, M., Van der Perre, G., Spaepen, A., Jonkers, I., 2008. Subject-specific hip geometry affects predicted hip joint contact forces during gait. Journal of Biomechanics 41, 1243-1252.

Marra, M.A., Vanheule, V., Fluit, R., Koopman, B.H., Rasmussen, J., Verdonschot, N., 2015. A Subject-Specific Musculoskeletal Modeling Framework to Predict in Vivo Mechanics of Total Knee Arthroplasty. Journal of Biomechanical Engineering 137, 020904.

Martelli, S., Valente, G., Viceconti, M., Taddei, F., 2014. Sensitivity of a subject-specific musculoskeletal model to the uncertainties on the joint axes location. Computer Methods in Biomechanics and Biomedical Engineering, 1-9.

Miranda, D.L., Rainbow, M.J., Leventhal, E.L., Crisco, J.J., Fleming, B.C., 2010. Automatic determination of anatomical coordinate systems for three-dimensional bone models of the isolated human knee. Journal of Biomechanics 43, 1623-1626.

Mirtich, B., 1996. Fast and Accurate Computation of Polyhedral Mass Properties. Journal of Graphics Tools 1, 31-50.

bioRxiv preprint doi: https://doi.org/10.1101/2020.06.23.162727; this version posted June 23, 2020. The copyright holder for this preprint (which was not certified by peer review) is the author/funder, who has granted bioRxiv a license to display the preprint in perpetuity. It is made available under aCC-BY-NC 4.0 International license.

Modenese, L., Caillet, A., Favier, C., Phillips, A., Kohout, J., Year Simulation of the hip muscles kinematics during gait using highly discretised anatomical models. In 26th Congress of the European Society of Biomechanics. Milan 2020 (Rescheduled due to COVID-19 pandemic, abstract available at https://simtk.org/projects/auto-sk-models).

Modenese, L., Ceseracciu, E., Reggiani, M., Lloyd, D.G., 2016. Estimation of musculotendon parameters for scaled and subject specific musculoskeletal models using an optimization technique. Journal of Biomechanics 49, 141-148.

Modenese, L., Jaere, M., Jones, G.G., Phillips, A., McGregor, A.H., Cobb, J.P., 2019. Integration of external knee joint loads in the pre-surgical planning of high tibial osteotomy: a proof-of-concept study XXVII Congress of the International Society of Biomechanics (ISB2019) and 43rd Annual Meeting of the American Society of Biomechanics (ASB2019), abstract available at https://simtk.org/projects/auto-sk-models, Calgary, Canada.

Modenese, L., Kohout, J., 2020. Automated Generation of Three-Dimensional Complex Muscle Geometries for Use in Personalised Musculoskeletal Models. Annals of Biomedical Engineering.

Modenese, L., Montefiori, E., Wang, A., Wesarg, S., Viceconti, M., Mazzà, C., 2018. Investigation of the dependence of joint contact forces on musculotendon parameters using a codified workflow for image-based modelling. Journal of Biomechanics 73, 108-118.

Montefiori, E., Modenese, L., Di Marco, R., Magni-Manzoni, S., Malattia, C., Petrarca, M., Ronchetti, A., de Horatio, L.T., van Dijkhuizen, P., Wang, A., 2019a. An image-based kinematic model of the tibiotalar and subtalar joints and its application to gait analysis in children with Juvenile Idiopathic Arthritis. Journal of biomechanics 85, 27-36.

Montefiori, E., Modenese, L., Di Marco, R., Magni-Manzoni, S., Malattia, C., Petrarca, M., Ronchetti, A., De Horatio, L.T., van Dijkhuizen, P., Wang, A., 2019b. Linking Joint Impairment and Gait Biomechanics in Patients with Juvenile Idiopathic Arthritis. Annals of biomedical engineering 47, 2155-2167.

Nardini, F., Belvedere, C., Sancisi, N., Conconi, M., Leardini, A., Durante, S., Parenti-Castelli, V., 2020. An Anatomical-Based Subject-Specific Model of In-Vivo Knee Joint 3D Kinematics From Medical Imaging. Applied Sciences 10, 2100.

Noguchi, S., Nishio, M., Yakami, M., Nakagomi, K., Togashi, K., 2020. Bone segmentation on whole-body CT using convolutional neural network with novel data augmentation techniques. Computers in Biology and Medicine 121, 103767.

Nolte, D., Ko, S.-T., Bull, A.M.J., Kedgley, A.E., 2020. Reconstruction of the lower limb bones from digitised anatomical landmarks using statistical shape modelling. Gait & Posture 77, 269-275.

Nolte, D., Tsang, C.K., Zhang, K.Y., Ding, Z., Kedgley, A.E., Bull, A.M.J., 2016. Non-linear scaling of a musculoskeletal model of the lower limb using statistical shape models. Journal of Biomechanics 49, 3576-3581.

Pitto, L., Kainz, H., Falisse, A., Wesseling, M., Van Rossom, S., Hoang, H., Papageorgiou, E., Hallemans, A., Desloovere, K., Molenaers, G., Van Campenhout, A., De Groote, F., Jonkers, I., 2019. SimCP: A Simulation Platform to Predict Gait Performance Following Orthopedic Intervention in Children With Cerebral Palsy. Frontiers in Neurorobotics 13.

Rainbow, M.J., Miranda, D.L., Cheung, R.T.H., Schwartz, J.B., Crisco, J.J., Davis, I.S., Fleming, B.C., 2013. Automatic determination of an anatomical coordinate system for a three-dimensional model of the human patella. Journal of Biomechanics 46, 2093-2096.

Renault, J.-B., Aüllo-Rasser, G., Donnez, M., Parratte, S., Chabrand, P., 2018. Articular-surface-based automatic anatomical coordinate systems for the knee bones. Journal of Biomechanics 80, 171-178.

Sancisi, N., Parenti-Castelli, V., 2011. A new kinematic model of the passive motion of the knee inclusive of the patella. Journal of Mechanisms and Robotics 3, 041003.

bioRxiv preprint doi: https://doi.org/10.1101/2020.06.23.162727; this version posted June 23, 2020. The copyright holder for this preprint (which was not certified by peer review) is the author/funder, who has granted bioRxiv a license to display the preprint in perpetuity. It is made available under aCC-BY-NC 4.0 International license.

Saxby, D.J., Modenese, L., Bryant, A.L., Gerus, P., Killen, B., Fortin, K., Wrigley, T.V., Bennell, K.L., Cicuttini, F.M., Lloyd, D.G., 2016. Tibiofemoral contact forces during walking, running and sidestepping. Gait & Posture 49, 78-85.

Scheys, L., Jonkers, I., Loeckx, D., Spaepen, A., Suetens, P., 2006. Automatic identification of muscle insertion sites in MR images using atlas-based, non-rigid registration. Gait & Posture 24, Supplement 2, S71-S72.

Scheys, L., Spaepen, A., Suetens, P., Jonkers, I., 2008. Calculated moment-arm and muscle-tendon lengths during gait differ substantially using MR based versus rescaled generic lower-limb musculoskeletal models. Gait & Posture 28, 640-648.

Seth, A., Hicks, J.L., Uchida, T.K., Habib, A., Dembia, C.L., Dunne, J.J., Ong, C.F., DeMers, M.S., Rajagopal, A., Millard, M., Hamner, S.R., Arnold, E.M., Yong, J.R., Lakshmikanth, S.K., Sherman, M.A., Ku, J.P., Delp, S.L., 2018. OpenSim: Simulating musculoskeletal dynamics and neuromuscular control to study human and animal movement. PLOS Computational Biology 14, e1006223.

Sholukha, V., Chapman, T., Salvia, P., Moiseev, F., Euran, F., Rooze, M., Jan, S.V.S., 2011. Femur shape prediction by multiple regression based on quadric surface fitting. Journal of Biomechanics 44, 712-718.

Smith, C.R., Won Choi, K., Negrut, D., Thelen, D.G., 2018. Efficient computation of cartilage contact pressures within dynamic simulations of movement. Computer Methods in Biomechanics and Biomedical Engineering: Imaging & Visualization 6, 491-498.

Stagni, R., Leardini, A., Cappozzo, A., Grazia Benedetti, M., Cappello, A., 2000. Effects of hip joint centre mislocation on gait analysis results. Journal of Biomechanics 33, 1479-1487.

Suwarganda, E.K., Diamond, L.E., Lloyd, D.G., Besier, T.F., Zhang, J., Killen, B.A., Savage, T.N., Saxby, D.J., 2019. Minimal medical imaging can accurately reconstruct geometric bone models for musculoskeletal models. PLOS ONE 14, e0205628.

Taddei, F., Martelli, S., Valente, G., Leardini, A., Benedetti, M.G., Manfrini, M., Viceconti, M., 2012. Femoral loads during gait in a patient with massive skeletal reconstruction. Clinical Biomechanics 27, 273-280.

Valente, G., Crimi, G., Vanella, N., Schileo, E., Taddei, F., 2017a. nmsBuilder: Freeware to create subject-specific musculoskeletal models for OpenSim. Computer Methods and Programs in Biomedicine 152, 85-92.

Valente, G., Pitto, L., Schileo, E., Piroddi, S., Leardini, A., Manfrini, M., Taddei, F., 2017b. Relationship between bone adaptation and in-vivo mechanical stimulus in biological reconstructions after bone tumor: A biomechanical modeling analysis. Clinical Biomechanics 42, 99-107.

Valente, G., Pitto, L., Testi, D., Seth, A., Delp, S.L., Stagni, R., Viceconti, M., Taddei, F., 2014. Are Subject-Specific Musculoskeletal Models Robust to the Uncertainties in Parameter Identification? PLoS ONE 9, e112625.

Victor, J., Premanathan, A., 2013. Virtual 3D planning and patient specific surgical guides for osteotomies around the knee: a feasibility and proof-of-concept study. The bone & joint journal 95, 153-158.

Winter, D.A., 2009. Biomechanics and motor control of the human movement, 4 ed. John Wiley & Sons, Waterloo, Ontario, Canada.

Yin, L., Chen, K., Guo, L., Cheng, L., Wang, F., Yang, L., 2015. Identifying the Functional Flexion-extension Axis of the Knee: An In-Vivo Kinematics Study. PloS one 10, e0128877.

Zhang, J., Fernandez, J., Hislop-Jambrich, J., Besier, T.F., 2016. Lower limb estimation from sparse landmarks using an articulated shape model. Journal of Biomechanics 49, 3875-3881.

Table 1 Joint coordinate systems and available algorithms to calculate their parameters. Kai-algorithms are described in Kai et al. (2014), GIBOC-algorithms are described in Renault et al. (2018), Miranda-algorithms are described in Miranda et al. (2010) and STAPLE-algorithms are described in the Supplementary Materials of this publication. Please note that the ground coordinate system coincides with that of the medical images in all models and that the algorithms used at the pelvis were always applied to bone geometries excluding the sacrum bone (considered challenging to segment in MRI scans). The algorithms applied to the "tibia" rigid body processed the geometry of the proximal tibia, full tibia or full tibia and fibula, depending on the algorithm. Note that the "foot" rigid body, including the geometries of calcaneus and foot bones, is called "calcn" in the OpenSim models for consistency with the other models included in the software distribution.

| **Rigid Body** | **Joint Coordinate System** | **Algorithms** | **Description of joint coordinate systems used for validation (from Modenese et al. 2018)** |
|---|---|---|---|
| pelvis | ground-pelvis child | Kai-Pelvis<br>STAPLE-Pelvis | Origin: midpoint of ASIS.<br>Axes: ISB recommendations for pelvis. |
| | hip parent | N/A | Origin: coincident with hip child origin.<br>Axes aligned with those of ground-pelvis child. |
| femur | hip child | Kai-Femur<br>GIBOC-Femur | Origin: center of femoral head (hip joint center).<br>Axes: defined as in ISB recommendations for femur. |
| | knee parent | Kai-Femur<br>Miranda-Femur<br>GIBOC-Spheres<br>GIBOC-Ellipsoids<br>GIBOC-Cylinder | Origin: the knee joint center, as defined by selected algorithm.<br>Axes: Z axis is the medio-lateral axis as defined by the selected algorithm.<br>Y axis is perpendicular to Z, lying in the same plane of Z and the hip joint center.<br>X axis is perpendicular to Y and Z. |
| tibia | knee child | Kai-Tibia<br>Miranda-Femur<br>GIBOC-Ellipse<br>GIBOC-Centroids<br>GIBOC-Plateau | Origin: coincident with knee parent origin.<br>Axes: Z axis aligned with medio-lateral axis of knee parent<br>Y axis is perpendicular to Z lying in the same plane as talocrural-child origin<br>X axis is perpendicular to Y and Z. |
| | talocrural parent | N/A | Origin: coincident with the talocrural child.<br>Axes: Z is aligned with the Z axis of the talocrural child.<br>Y axis is perpendicular to Z, lying in the same plane of Z and the knee joint center.<br>X axis is perpendicular to Y and Z. |
| talus | talocrural child | STAPLE-Talus | Origin: point at midpoint of the length on the axis of the cylinder fitter to the talar trochlea articular surface.<br>Axes: Z is the axis of the cylinder fitted to the talar trochlea articular surface.<br>X is perpendicular to Z, lying on a plane parallel to the foot sole XZ plane.<br>Y is perpendicular to X and Z. |
| | subtalar parent | STAPLE-Talus | Origin: center of the sphere fitted to the articular surface of the talocalcaneal joint.<br>Axes: Z axis on the line from the center of sphere fitted to the talocalcaneal articular surface to that fitted to the talonavicular articular surface.<br>Y is perpendicular to Z, lying in the same plane of Z and the knee joint centre.<br>X axis is perpendicular to Y and Z. |
| foot | subtalar child | N/A | Origin and axes defined by subtalar parent. |
| | foot sole (auxiliary) | STAPLE-Foot | Origin: most distal point of the calcaneus.<br>Axes: X axis pointing from the most caudal point on the talus to the midpoint of the most caudal points on the 1$^{st}$ and 5$^{th}$ metatarsal heads.<br>Y axis perpendicular to the plane identified by the points defining X.<br>Z axis is perpendicular to X and Y. |

bioRxiv preprint doi: https://doi.org/10.1101/2020.06.23.162727; this version posted June 23, 2020. The copyright holder for this preprint (which was not certified by peer review) is the author/funder, who has granted bioRxiv a license to display the preprint in perpetuity. It is made available under aCC-BY-NC 4.0 International license.

Table 2 Landmarks identified on the three-dimensional bone geometries by the automated algorithms.

| Rigid Body | Bony landmark | Description |
|---|---|---|
| pelvis | ASI | Anterior superior iliac spine |
| | PSI | Posterior superior iliac spine |
| femur | TRO | Great trochanter |
| | MFC | Medial femoral epicondyle |
| | KNE | Lateral femoral epicondyle |
| tibia/fibula | MMA | Medial malleolus |
| | ANK | Lateral malleolus |
| | TTB | Tibial tuberosity |
| | HFB | Fibular head |
| foot | D1M | Head of first metatarsal bone |
| | D5M | Head of fifth metatarsal bone |
| | HEE | Heel |

bioRxiv preprint doi: https://doi.org/10.1101/2020.06.23.162727; this version posted June 23, 2020. The copyright holder for this preprint (which was not certified by peer review) is the author/funder, who has granted bioRxiv a license to display the preprint in perpetuity. It is made available under aCC-BY-NC 4.0 International license.

Table 3 Description of the anatomical datasets employed in the current study. Please note that the LHDL-CT and ICL-MRI bone geometries were pre-processed using MeshLab. The details of the medical images are presented as reported in the reference publications.

| Dataset | Gender | Age | Height [m] | Mass [kg] | MSK conditions | Imaging type | Details of medical images | Quality of bone geometry | Reference publication (R)/ previous use in the authors' work (U) |
|---|---|---|---|---|---|---|---|---|---|
| LHDL-CT | F | 78 | 1.71 | 64 | No | CT | CT scans collected with Siemens Sensation 64, pixel spacing and slice thickness: 0.98 mm x 0.98 mm x 1.0 mm, 1 mm slice spacing. | Very Good | R: Viceconti et al. (2008)<br>U: Modenese et al. (2016, 2019), Modenese et Kohout (2020) |
| TLEM2-CT | M | 85 | N/A | 45* | No | CT | CT scans collected with Siemens SOMATOM® Sensation 16 CT Scanner, voxel size of 0.977 mm x 0.977mm x 0.75 mm. | Good | R: Carbone et al. (2015)<br>U: Modenese et al. (2019) |
| ICL-MRI | M | 38 | 1.80 | 87 | No | MRI | 3D T1-weighted VIBE, axial field of view: 450x450 mm, pixel size: 1.41x1.41 mm, slice thickness and increment: 1 mm | Average | R/U: Modenese et al. (2020) |
| JIA-MRI** | M | 14 | 1.74 | 76.5 | JIA*** | MRI | 3D T1-weighted fat-suppression sequence (e-THRIVE) with 1 mm in-plane resolution and 1 mm slice thickness. | Low | R/U: Montefiori et al. 2019b |

* estimated by Carbone et al. (2015).

** the OpenSim model, but not the medical images, is available with the reference publication.

*** this model represents an individual affected by rheumatoid-factor-negative polyarticular juvenile idiopathic arthritis with no signs of inflammation at the time of MRI scans (patient P3 in Montefiori et al. 2019b).

bioRxiv preprint doi: https://doi.org/10.1101/2020.06.23.162727; this version posted June 23, 2020. The copyright holder for this preprint (which was not certified by peer review) is the author/funder, who has granted bioRxiv a license to display the preprint in perpetuity. It is made available under aCC-BY-NC 4.0 International license.

Table 4 Differences between the joint coordinate systems in the manual and automatic skeletal models. The automatic models were created using the algorithms STAPLE-Pelvis, GIBOC-Femur, Kai-Tibia, STAPLE-Talus and STAPLE-Foot. Linear distances between the origins of the joint coordinate systems are expressed in the reference system of the medical images, for which axes directions are: Z pointing cranially, Y posteriorly, X to the left for LHDL-CT, TLEM2-CT and JIA-MRI; Z pointing cranially, Y anteriorly and X to the right for ICL-MRI.

| Dataset | Joint | Origin displacement vector [mm] | | | | Axes Differences - Parent [deg] | | | Axes Differences - Child [deg] | | |
|---|---|---|---|---|---|---|---|---|---|---|---|
| | | X | Y | Z | norm | X | Y | Z | X | Y | Z |
| LHDL-CT | pelvis-ground | -0.7 | 0.8 | -3.0 | 3.1 | 0.0 | 0.0 | 0.0 | 3.1 | 3.4 | 1.2 |
| | hip | -0.2 | -0.2 | 0.2 | 0.3 | 3.1 | 3.4 | 1.2 | 0.7 | 0.2 | 0.7 |
| | knee | -0.8 | 1.0 | 0.2 | 1.3 | 0.7 | 0.4 | 0.7 | 0.6 | 0.4 | 0.7 |
| | talocrural | 0.1 | 0.3 | -0.9 | 0.9 | 0.2 | 0.4 | 0.5 | 1.7 | 1.7 | 0.5 |
| | subtalar | -0.3 | 0.3 | 0.0 | 0.4 | 0.8 | 2.6 | 2.7 | 0.8 | 2.6 | 2.7 |
| TLEM2-CT | pelvis-ground | -1.0 | 0.2 | -4.9 | 5.0 | 0.0 | 0.0 | 0.0 | 3.4 | 3.5 | 0.9 |
| | hip | -0.1 | -0.1 | 0.2 | 0.3 | 3.4 | 3.5 | 0.9 | 0.1 | 0.2 | 0.2 |
| | knee | 1.0 | -0.3 | 0.2 | 1.1 | 0.1 | 0.2 | 0.2 | 0.2 | 0.3 | 0.2 |
| | talocrural | 0.1 | -0.9 | 0.4 | 1.0 | 0.7 | 0.7 | 1.0 | 1.9 | 1.6 | 1.0 |
| | subtalar | -0.1 | 1.0 | -0.1 | 1.0 | 0.3 | 2.1 | 2.0 | 0.3 | 2.1 | 2.0 |
| ICL-MRI | pelvis-ground | -0.5 | 0.0 | 0.8 | 0.9 | 0.0 | 0.0 | 0.0 | 1.8 | 2.0 | 1.0 |
| | hip | 0.0 | 0.1 | 0.1 | 0.1 | 1.8 | 2.0 | 1.0 | 0.1 | 2.0 | 2.0 |
| | knee | 2.0 | 0.5 | 1.4 | 2.5 | 0.1 | 0.1 | 0.1 | 0.2 | 0.2 | 0.1 |
| | talocrural | 0.7 | -0.6 | 0.0 | 0.9 | 0.3 | 0.4 | 0.4 | 2.5 | 2.6 | 0.4 |
| | subtalar | -0.2 | -2.8 | -1.4 | 3.2 | 0.3 | 2.9 | 2.9 | 0.3 | 2.9 | 2.9 |
| JIA-MRI | pelvis-ground | 0.5 | 1.0 | -4.4 | 4.5 | 0.0 | 0.0 | 0.0 | 3.4 | 3.6 | 1.0 |
| | hip | -0.2 | 0.1 | -0.4 | 0.5 | 3.4 | 3.6 | 1.0 | 0.9 | 0.1 | 0.9 |
| | knee | 0.3 | -0.2 | -1.0 | 1.1 | 0.9 | 0.1 | 0.9 | 0.9 | 0.1 | 0.9 |
| | talocrural | -0.2 | 0.1 | 1.2 | 1.2 | 3.0 | 3.0 | 0.2 | 2.1 | 2.1 | 0.2 |
| | subtalar | -1.4 | -0.4 | -5.7 | 5.9 | 2.2 | 11.3 | 11.3 | 2.2 | 11.3 | 11.3 |

bioRxiv preprint doi: https://doi.org/10.1101/2020.06.23.162727; this version posted June 23, 2020. The copyright holder for this preprint (which was not certified by peer review) is the author/funder, who has granted bioRxiv a license to display the preprint in perpetuity. It is made available under aCC-BY-NC 4.0 International license.

bioRxiv preprint doi: https://doi.org/10.1101/2020.06.23.162727; this version posted June 23, 2020. The copyright holder for this preprint (which was not certified by peer review) is the author/funder, who has granted bioRxiv a license to display the preprint in perpetuity. It is made available under aCC-BY-NC 4.0 International license.

Table 5 Comparison among the joint coordinate systems estimated by all the available algorithms and the one used in the validation step, considered as reference algorithm. Components of the displacement vectors are expressed in the joint coordinate system of the reference algorithm. N/S means "not solved" and indicates that the algorithm crashed or computed a manifestly incorrect solution.

| **Joint Coordinate System [Reference Algorithm]** | **Algorithm** | **Dataset** | **Origin displacement vector [mm]** | | | | **Axes Differences [deg]** | | |
|---|---|---|---|---|---|---|---|---|---|
| | | | **X** | **Y** | **Z** | **norm** | **X** | **Y** | **Z** |
| ground-pelvis-child [STAPLE-Pelvis] | Kai-Pelvis | LHDL-CT | -0.4 | 5.7 | 0.5 | 5.7 | 2.3 | 2.4 | 0.8 |
| | | TLEM2-CT | -0.2 | 1.1 | -0.2 | 1.1 | 0.5 | 0.7 | 0.5 |
| | | ICL-MRI | -1.3 | 5.8 | -0.1 | 6.0 | 2.1 | 2.4 | 1.3 |
| | | JIA-MRI | -0.1 | 0.4 | 0.1 | 0.4 | 0.2 | 0.2 | 0.2 |
| Knee-parent [GIBOC-Cylinder] | Miranda-Femur* | LHDL-CT | 0.6 | -1.4 | -0.2 | 1.6 | 2.9 | 2.6 | 1.5 |
| | | TLEM2-CT | -3.2 | -1.7 | 0.4 | 3.7 | 0.7 | 0.9 | 0.6 |
| | | ICL-MRI | N/S | N/S | N/S | N/S | N/S | N/S | N/S |
| | | JIA-MRI | N/S | N/S | N/S | N/S | N/S | N/S | N/S |
| | Kai-Femur | LHDL-CT | -2.4 | -0.3 | 0.9 | 2.5 | 3.6 | 3.0 | 4.7 |
| | | TLEM2-CT | -3.8 | -0.8 | 0.6 | 4.0 | 3.0 | 0.6 | 3.0 |
| | | ICL-MRI | -3.8 | -1.0 | -0.1 | 3.9 | 3.6 | 2.8 | 4.5 |
| | | JIA-MRI | -3.6 | -1.1 | 0.0 | 3.7 | 1.9 | 1.5 | 2.2 |
| | GIBOC-Spheres | LHDL-CT | 0.0 | -0.5 | 1.4 | 1.5 | 0.1 | 0.1 | 0.1 |
| | | TLEM2-CT | 0.9 | 0.1 | 2.0 | 2.2 | 0.2 | 0.2 | 0.2 |
| | | ICL-MRI | 0.0 | -0.6 | 1.3 | 1.4 | 0.6 | 0.5 | 0.8 |
| | | JIA-MRI | -1.3 | -1.4 | 2.2 | 2.8 | 5.0 | 4.6 | 6.7 |
| | GIBOC-Ellipsoids | LHDL-CT | 9.1 | 1.2 | 1.2 | 9.3 | 4.4 | 2.3 | 4.5 |
| | | TLEM2-CT | 8.6 | -0.4 | 2.0 | 8.8 | 4.4 | 3.6 | 5.2 |
| | | ICL-MRI | 9.0 | 0.4 | 1.6 | 9.2 | 3.6 | 1.9 | 3.6 |
| | | JIA-MRI | 7.8 | 1.2 | 2.1 | 8.1 | 2.6 | 3.0 | 3.4 |
| Knee-child [Kai-Tibia] | Miranda-Tibia** | LHDL-CT | -0.1 | 7.5 | -1.7 | 7.7 | 10.9 | 7.0 | 9.9 |
| | | TLEM2-CT | N/S | N/S | N/S | N/S | N/S | N/S | N/S |
| | | ICL-MRI | -0.5 | 8.7 | -1.5 | 8.8 | 7.8 | 5.4 | 5.7 |
| | | JIA-MRI | 0.6 | 0.3 | 0.5 | 0.8 | 4.4 | 3.8 | 2.9 |
| | GIBOC-Plateau | LHDL-CT | -1.7 | 10.4 | -1.2 | 10.6 | 9.3 | 1.7 | 9.1 |
| | | TLEM2-CT | -0.9 | 10.3 | -1.6 | 10.5 | 2.7 | 0.9 | 2.6 |
| | | ICL-MRI | -1.8 | 12.5 | -2.2 | 12.9 | 6.0 | 1.8 | 5.8 |
| | | JIA-MRI | -1.4 | 6.2 | -1.3 | 6.5 | 5.4 | 1.4 | 5.2 |
| | GIBOC-Ellipse | LHDL-CT | -3.5 | 10.1 | -2.1 | 10.9 | 2.8 | 2.1 | 1.9 |
| | | TLEM2-CT | -2.6 | 10.0 | -2.8 | 10.7 | 4.0 | 1.2 | 3.8 |
| | | ICL-MRI | -4.9 | 12.1 | -2.7 | 13.3 | 2.6 | 2.3 | 1.3 |
| | | JIA-MRI | -4.5 | 5.8 | 0.1 | 7.4 | 6.7 | 2.0 | 6.4 |
| | GIBOC-Centroids | LHDL-CT | -2.1 | 10.4 | -1.6 | 10.7 | 1.9 | 1.8 | 0.5 |
| | | TLEM2-CT | -2.4 | 10.0 | -1.5 | 10.4 | 2.3 | 1.2 | 2.0 |
| | | ICL-MRI | -8.7 | 11.7 | -2.8 | 14.8 | 4.2 | 2.9 | 3.2 |
| | | JIA-MRI | -3.3 | 6.0 | 0.0 | 6.9 | 11.7 | 1.8 | 11.5 |

* Miranda-Femur crashed when processing JIA-MRI and fitted the shaft of the femur of ICL-MRI.

**Miranda-Tibia identified inverted axes direction for TLEM2-CT and was not able to process the JIA-MRI tibial geometry unless the fibula was included as well.